Characterization of the new Ultracold Neutron beamline at the LANL UCN facility

D. K.-T. Wong^{a,b,*}, M. T. Hassan^b, J. F. Burdine^b, T. E. Chupp^c, S. M. Clayton^b, C. Cude-Wood^{b,d}, S. A. Currie^b, T. M. Ito^{b,*}, C.-Y. Liu^a, M. Makela^b, C. L. Morris^b, C. M. O'Shaughnessy^b, A. Reid^a, N. Sachdeva^{c,e}, W. Uhrich^b

> ^aIndiana University, Bloomington, Indiana 47405, USA ^bLos Alamos National Laboratory, Los Alamos, New Mexico 87545, USA ^c University of Michigan, Ann Arbor, Michigan, 48109, USA ^dNorth Carolina State University, Raleigh, North Carolina, 27695, USA ^eNorthwestern University, Evanston, Illinois, 60208, USA

Abstract

The neutron electric dipole moment (nEDM) experiment that is currently being developed at Los Alamos National Laboratory (neutrons) (uCNs) and Ramsey's method of separated oscillatory fields to search for a nEDM. In this paper, we present measurements of UCN storage and UCN transport during the commissioning of a new beamline at the LANL UCN we also present an analytical model describing data that provides a simple parameterization of the input UCN energy spectrum on the new beamline.

Keywords: ultracold neutrons, neutron electric dipole moment**

Introduction

Ultracold neutrons (UCNs) [1, 2] are neutrons of sufficiently low kinetic energy (5440 nev) that they can be confined in material or magnetic bottles. UCNs are playing increasingly important class of fundamental physical interactions (for recent reviews, see e.g. Refs. [3, 4]).

One particularly important class of experiments performed using UCNs is the search for a nonzero electric dipole moment of the neutron (nEDM) (see e.g. Refs. [5, 6]), which probes new sources of time reversal symmetry violation [7, 8, 9] and may give clues to the puzzle of the matter-antimatter asymmetry in the universe [10, 11]. Modern nEDM experiment; which consists of the following steps, will be repeated many time over the course of the experiment: 1) UCNs are loaded into the precession cells.

At Los Alamos National Laboratory (LANL), a solid deuterium (SD₂) based superthermal UCN source based into the respective property of the precession sell.

At Los Alamos National Laboratory (LANL), a solid deuterium (SD₂) based superthermal UCN source based into the respective property of the precessively been upgraded to host a new nEDM experiment that will use Ramburger and the property of the precession cell (i.e., how the stored UCN source performance and UCN transport. Both and figure and the continuation of the experiment, a result of UCN source performance and UCN transport. Both and there are several elforts worldwide aimed at searching for the new new performance a

verter as well as the cold neutron moderator, was replaced with an improved design. The upgrade produced a factor of four increase in UCN density [15].

$$\sigma_{d_n} = \frac{\hbar}{2\alpha E T_{\rm fp} \sqrt{N}},\tag{1}$$

loss properties of the cell. The operating condition (how long to load the cell, how long to store the UCN, and how long to unload the cell, etc) needs optimized to minimize the uncertainty of the experiment. Therefore our measurements were focused on characterizing the UCN density and energy spectrum at the location of the experiment, as well as the UCN storage property of the precession cell.

^{*}Corresponding authors Email addresses: dkwong@iu.edu (D. K.-T. Wong), ito@lanl.gov

In this paper, we describe the measurements performed, present the results and analysis, and demonstrate an analytical model to quantify the collected data.

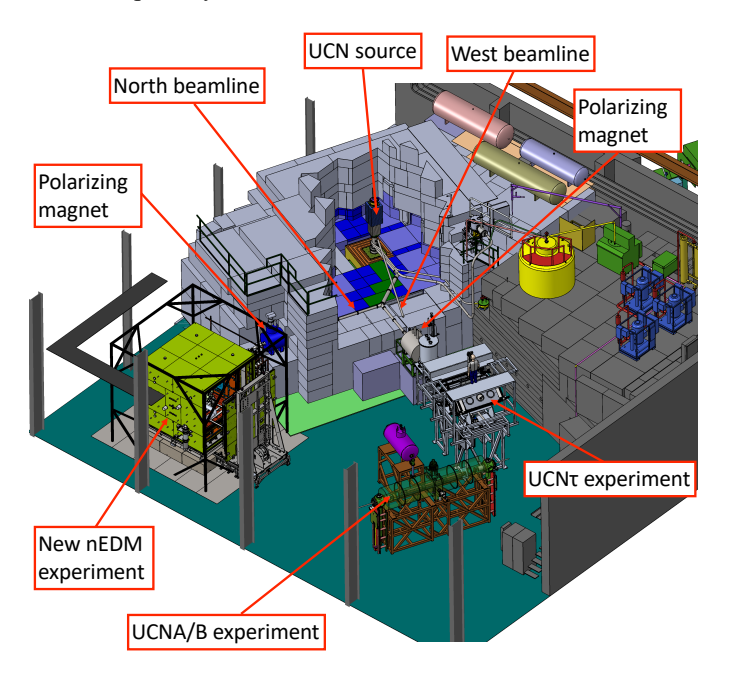


Figure 1: Schematic of the experimental area at the LANL UCN facility

2. Description of experimental setup

The schematic diagram of the experimental setup mounted on the North Beamline is shown in Fig. 2. There were two gate valves (GV) located on the beamline, with a 6.35 mm-diameter "monitor port" located in between. UCN that traveled through the monitor port were counted with a ^{10}B coated ZnS:Ag detector [16]. The rate of UCN through the monitor port is proportional to the UCN density in the guides (in the case of an isotropic distribution, the rate *R* through the monitor port hole with an area *A* and the UCN density ρ are related via $R = \frac{1}{4}\bar{\nu}\rho A$, where $\bar{\nu}$ is the average UCN speed, *i.e.* $\bar{\nu} = \int \nu f(\nu) d\nu$, with f describing the UCN velocity distribution). Hence, the rate of the monitor detector gives the approximate rate of the UCN in the guide.

A 5 T, horizontal warm bore, superconducting magnet by American Magnetics Inc. was used as a polarizing magnet (PM). The strong magnetic field from the PM interacts with the neutron magnetic moment creating a potential given by $-\vec{\mu}_n \cdot \vec{B}$, where $\vec{\mu}_n$ is the neutron magnetic moment and \vec{B} is the magnetic field. The PM field is effectively a UCN spin filter, acting as a potential barrier that rejects low-field seeking UCN below 300 neV and a potential well that passes high-field seeking UCN. For the measurements described in this paper, we varied \vec{B} for the purpose of obtaining information on the UCN spectrum

A thin (0.0762 mm) Al foil, termed the "PM window", is located in the beamline at the center of the PM field region. This is used to separate the UCN source vacuum from the measurement apparatus vacuum, as small vacuum excursions in the

source due to beam heating would spoil the cell vacuum and shorten its lifetime. The magnetic potential of the PM overwhelms the Fermi potential of the window (54 neV). The effect of the window on the transmission of UCN is discussed in detail in section 4.

A UCN switcher was located downstream of the PM. The switcher directed UCN from the source to the cell (fill mode) or from the cell to a UCN spin analyzer and detector (counting mode). In the counting mode, UCN were sent to a "drop-detector" located below beam height. Two types of switchers were utilized for the measurements described in this paper. The first one was termed the "prototype switcher," and the second, which will be used for the eventual LANL nEDM experiment, was termed the "rotary switcher."

The rotary switcher has a cylindrical housing and four evenly spaced guide ports. These guide ports could be connected by either a straight guide section or 90° bend sections. All guide sections inside were mounted on a rotating turntable and actuated by a Parker CM232DX servo-motor. An image of the rotary switcher as well as a schematic of the guide segments within it are shown in Fig. 3 and 4.

All guide sections downstream of the PM had a 50 μ m-thick electroless nickel phosphorus (NiP) coating. NiP has a high UCN storage Fermi potential of 213(5) neV, a low spin-flip per bounce probability of $3.6(5) \times 10^{-6}$, and a low UCN loss probability of $1.3(1) \times 10^{-4}$ per bounce [17, 18]. To adiabatically transport neutron spins, the guides downstream of the PM were kept under a ~1 mT magnetic field produced by coils.

On both the monitor and the drop-detector, ^{10}B coated ZnS:Ag scintillator films were used for UCN detection [16]. UCNs were captured on the top layer of ^{10}B , and reaction products (4 He and/or 7 Li) from the $^{10}B(n,\alpha)^{7}$ Li neutron capture reaction were detected in the ZnS:Ag layer. The resulting scintillation light was then detected by a photomultiplier tube (PMT). The photocathode diameters of the drop-detector and monitor detector PMTs were 76.2 mm and 28.6 mm, respectively.

A neutron spin analyzer that consisted of a 10 layer polarizer made of iron and silicon was located immediately above the drop detector (see Ref. [19] for layer structure details). When magnetized with a 10 mT field from permanent magnets, the multi-layer polarizer preferentially transmitted high-field seeking UCN and rejected low-field seeking UCN with an analyzing power of 99.0^{+0.7}_{-2.4}% [19]. Additionally, an adiabatic fast passage (AFP) spin flipper coil, located upstream of the spin analyzer, was used to provide the option of spin flipping UCN [20]. A schematic of the analyzer system is illustrated in Fig. 5

UCN were stored in cylindrical cell with an inner diameter of 50 cm and a height of 10 cm, giving a total volume of 19.6 L. Several different configurations for the prototype cell were used in the measurements for this paper and are discussed in further detail in section 3.1. The bottom of the cell was located approximately 10 cm above beamline guide height.

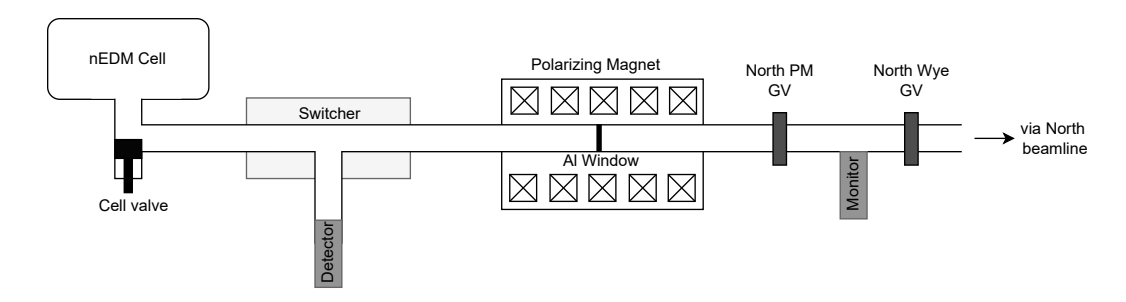


Figure 2: Layout of the North Beamline



Figure 3: A photograph of the rotary switcher

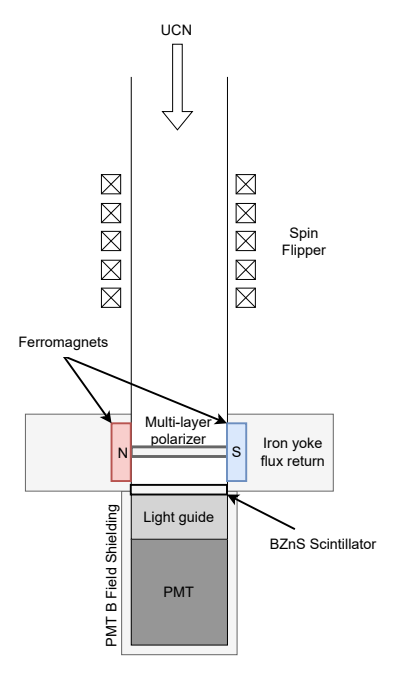


Figure 5: Schematic of the adiabatic fast passage (AFP) spin flipper, spin analyzer, and UCN detector system

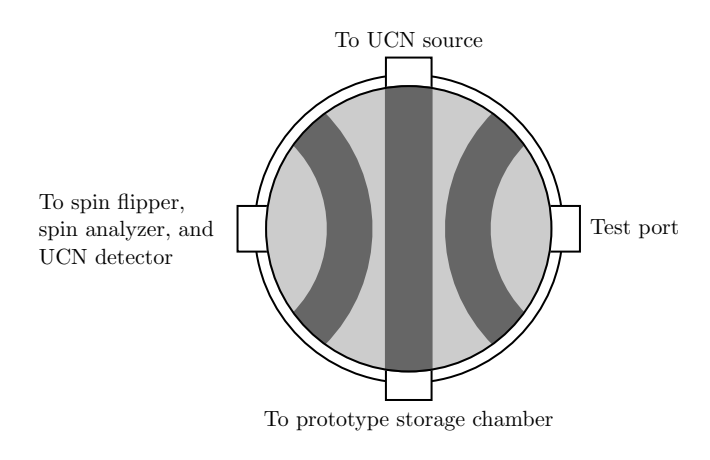


Figure 4: A top-down schematic of the rotary switcher

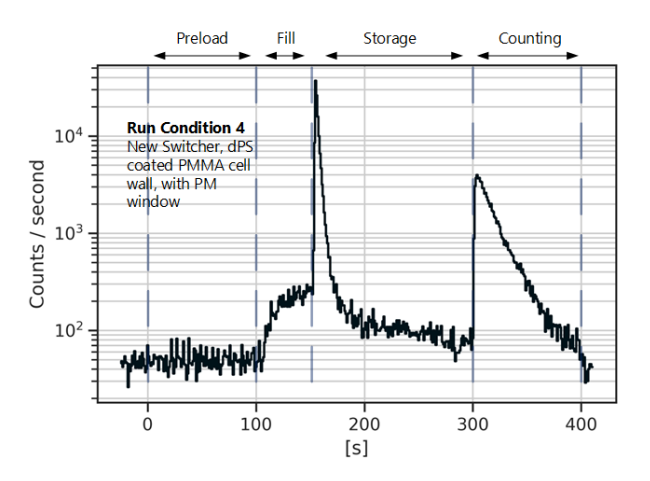


Figure 6: UCN count rate during the "fill-and-dump" measurement sequence for one run. Preload: $0\,s$ to $100\,s$. Filling period: $100\,s$ to $150\,s$. Holding period: $150\,s$ to $300\,s$. Counting period: $300\,s$ to $400\,s$.

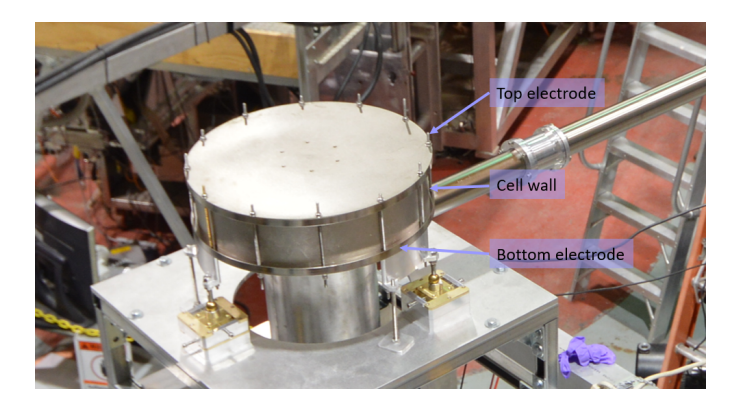


Figure 7: A photograph of a prototype precession cell (pictured here with NiPcoated Al cell walls)

3. Measurements

3.1. Measurement of UCN storage time

A UCN storage lifetime measurement was performed using a "fill-and-dump" method. The steps were: (1) The North Wye GV was opened while the North PM GV was kept closed for 100 s to "preload" the UCN to build up UCN density behind the GV. (2) The North PM GV was opened, allowing UCN to pass through the PM and the switcher into the nEDM cell. This filling period was 50 s. (3) The cell valve and North PM GV were closed to stop the flow of UCN into the precession cell. (4) The cell valve was kept closed for some "holding time" to store UCN. (5) The switcher moved from the fill mode to count mode in preparation to empty the precession cell. (6) The cell valve was opened to allow UCN to flow to the drop detector. This counting period lasted for 100 s. Note that for these of measurements, the UCN final spin was not measured. See Fig. 6 for the drop detector UCN count rate for one such run.

Two different types of precession cell walls were tested: (i) NiP coated Al and (ii) deuterated polystyrene (dPS) coated poly(methyl methacrylate) (PMMA). In both cases, the top and bottom surfaces of the cell were NiP coated Al. In the final nEDM experiment the dPS-coated PMMA cell wall will be used in combination with nickel-molybdenum-coated top and bottom plates (which will be used as high voltage electrodes). A photograph of the prototype cell is shown in Fig. 7.

Fill-and-dump holding time scans were repeated for holding times of 30 to 300 seconds. Holding time scans were repeated with PM strengths of 0 T, 1.25 T, 2.5 T, 3.75 T and 5 T. An overview of UCN hold-time run conditions is summarized in Tab. 1. It should be noted that for run condition 1, the UCN source was run continuously and the GV was simply opened and closed between fill-and-dump measurements. To avoid delivering beam to the target unnecessarily, run conditions 2-4 switched to a mode where the beam was on only during preload and filling periods.

3.2. Measurement of spin dependent UCN flux transmission rate as a function of PM field

Direct "flow-through" measurements of UCN transmission through the PM were taken to provide information on the incoming UCN energy spectrum. During these measurements, the magnetic field of the PM was slowly decreased from 5 T to 0 T over the course of 72 min (28 min to ramp from 5 T to 4.11 T, 44 min to ramp from 4.11 T to 0 T). UCN transported from a continuous source to the drop detector, while UCN were spin flipped every 67 s by the AFP spin flipper described in section 2. These measurements were repeated for configurations both with and without the Al window installed in the PM region. Analysis of this data is presented in section 4.3.

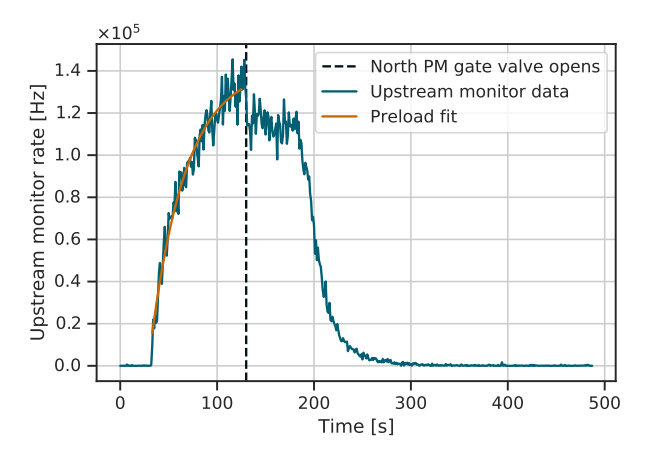


Figure 8: An illustration of a preload fit used for normalization under run conditions 2-4, as described in section 4.1. Data in this figure is obtained from an upstream monitor located on the "West Beamline". UCN density is built up behind a stainless steel gate valve for $100\,\mathrm{s}$. The gate valve is then opened to allow UCN to fill the precession cell on the north beamline, causing a dip on the upstream monitor rate

4. Data Analysis and Modeling

4.1. Data processing and normalization

In order to generate a reliable UCN storage time curve, it is necessary to subtract background and normalize UCN counts to correct for variations in UCN source intensity.

A monitor upstream of the PM located on the "West Beamline" (see Fig. 1) was used to normalize the number of UCN measured by the drop detector during the counting period. The upstream monitor measured a UCN count rate of ~ 2000 UCN/s (North PM GV closed) when beam and source parameters were optimally tuned. This monitor rate corresponded to a density of 184(32) UCN/cm³ at the exit of the biological shield [15].

The UCN rate measured in the West Beamline monitor as a function of time during the preload, R(t), was fit to the form of an exponential, $R(t) = A(1 - \exp[-(t - t_0)/\tau])$ to determine free parameters A, t_0 , and τ for conditions 2-4 in table 1. The scaling factor to obtain a normalized UCN count is then given by 2000/R(100), the rate at the end of the preload period. An example of a preload fit utilized for normalization is illustrated in Fig. 8. For run condition 1, R was taken to be the average value of the West Beamline monitor rate during the preload period because the beam was not turned off during the measurement run. The PMT background rate for each data set was fitted and subtracted from the UCN counting period.

Table 1: Switcher, cell wall, and PM window conditions for measurements

#	Run Condition	Storage Curve
1	Prototype switcher, NiP coated Al cell wall, no PM window	Fig. 10
2	Prototype switcher, NiP coated Al cell wall, with PM window	Fig. 11
3	Rotary switcher, NiP coated Al cell wall, with PM window	Fig. 12
4	Rotary switcher, dPS coated PMMA cell wall, with PM window	Fig. 13

During analysis, it was discovered that some portion of UCN storage runs had a small leakage of UCN during the storage period, a result of the cell valve not fully closing. Typically, in a leak-less run, UCN remaining in the guide system after the filling period drained into the drop-detector in the first $\sim 20\,\mathrm{s}$ of the holding period. This "guide-dump" count of UCN could be fit with a single decaying exponential and typically exhibited a decay time on the order of one or two seconds. However, with a leak, a double exponential function was observed with a secondary decay on the order of $\sim 50\,\mathrm{s}$.

The leak-corrected count of UCN, N_{cc} , was obtained from the uncorrected count of UCN, N_{c} , with

$$N_{\rm cc} = N_{\rm c} + \int_{t_1}^{t_2} dt \int_{t_2}^{t_3} dt' f(t)g(t')e^{-(t'-t)/\tau}$$
 (2)

where, as illustrated in Fig. 9, t_1 is the start of the holding period, t_2 is the start of the counting period, and t_3 is the end of the counting period. The number of leaked UCN at a given time, f(t), was obtained by fitting the guide dump on leak-free runs, and then subtracting the fit from runs with leaks. The rate of UCN detected at time t during the counting period from the cell dump, g(t), is normalized such that $\int g(t)dt = 1$. The exponential term approximates the decay of stored UCNs, where τ is the effective decay constant determined by fitting to the uncorrected storage curve.

The size of the leak correction varied. It was smaller for shorter holding time runs (< 2% of counted UCNs for storage times less than 50 s), and was larger for longer hold runs (up to 10% of counted UCNs for storage times of 300 s). The uncertainty of the leak correction was less than 5% of the leak correction, and therefore the contribution to the total measurement uncertainty was negligibly small. The normalized UCN counts thus obtained are plotted in Fig. 10-13.

4.2. UCN storage curves in prototype precession cells

In this section we introduce an analytical model to fit UCN lifetime storage curves in the precession cell, with parameters that describe properties of the UCN storage vessel, physical parameters of the neutron velocity spectrum upstream of the PM, and the effect of the PM on the spectrum. This model can be used to quickly obtain physical information from UCN storage curves without the need to create a comprehensive Monte Carlo simulation of a system, which can be labor intensive and computationally costly.

It is a common practice to fit UCN storage lifetime measurements to single-exponential curves, which is only correct for

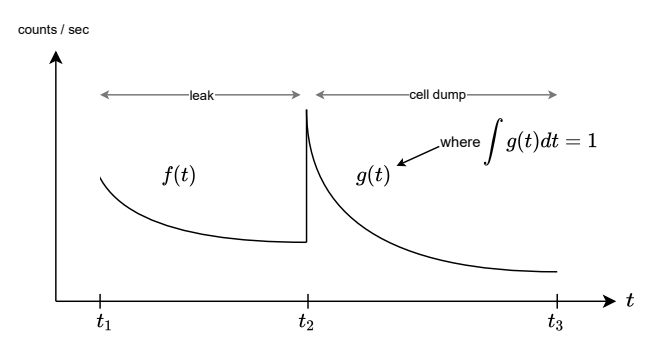


Figure 9: Visualization of parameters used for leak correction of UCN storage in Eq. (2), as referred to in section 4.1

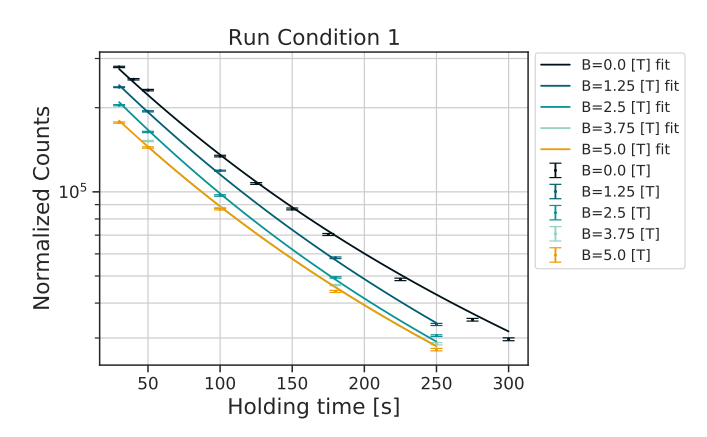


Figure 10: UCN storage measurement run condition 1: Prototype switcher, NiP coated Al cell wall, no PM window. Data normalization on the y-axis is discussed in section 4.1. Fits of UCN storage measurements described in section 3. Fit results are described in Tab. 2.

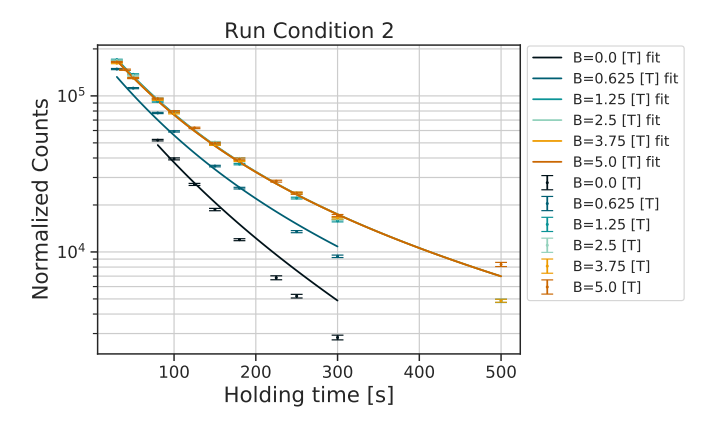


Figure 11: UCN storage measurement run condition 2: Prototype switcher, NiP coated Al cell wall, with PM Window. Data normalization on the y-axis is discussed in section 4.1. Fits of UCN storage measurements described in section 3. Fit results are described in Tab. 2.

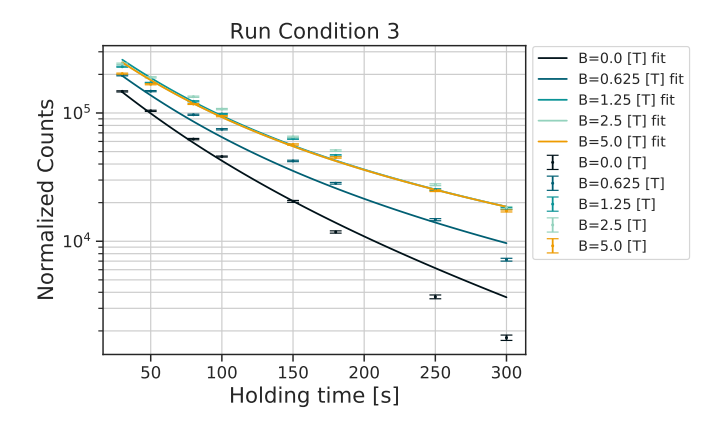


Figure 12: UCN storage measurement run condition 3: Rotary Switcher, NiP coated Al cell wall, with PM window. Data normalization on the y-axis is discussed in section 4.1. Fits of UCN storage measurements described in section 3. Fit results are described in Tab. 2.

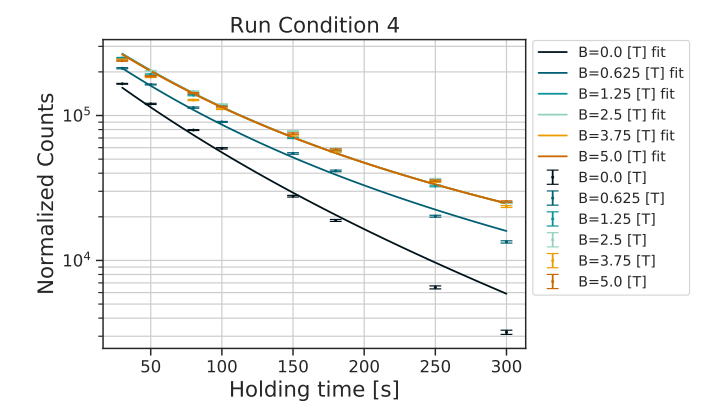


Figure 13: UCN storage measurement run condition 4: Rotary Switcher, dPS coated PMMA cell wall, with PM window. Data normalization on the y-axis is discussed in section 4.1. Fits of UCN storage measurements described in section 3. Fit results are described in Tab. 2.

single velocity spectra. However, the velocity spectrum of a population of UCN is a continuous distribution. Double exponential curves are often used to effectively represent such decay curves made of multiple velocity components, but it is not ideal.

Let dN_0/dv be the UCN velocity spectrum upstream of the PM, and dN_1/dv be the UCN velocity spectrum downstream of the PM. As the starting point, for simplicity, assume the following functional forms:

$$\frac{dN_0}{dv} \propto v^{\alpha} \tag{3}$$

$$\frac{dN_0}{dv} \propto v^{\alpha} \tag{3}$$

$$\frac{dN_1}{dv} = \frac{1}{2} \frac{dN_0}{dv} (f_h + f_\ell) \tag{4}$$

where α is a free parameter of the model. Equation (3) is a functional form for the velocity distribution of the UCN transported from the source to the location of the experiment, as utilized in Ref. [15]. f_h and f_ℓ are the fraction of high-field seekers and low-field seekers transmitted through the PM, respectively. Here, we assume that UCN are completely unpolarized upstream of the PM.

In the situation with no window present in the center of the PM, the PM passes all the high field seeking neutrons with $v_{\parallel} > 0$, where v_{\parallel} is the longitudinal velocity along the axis of the UCN guide. The PM passes low field seeking neutrons for $v_{\parallel} > 0$ only if $\frac{1}{2}m_n(v_{\parallel})^2 > \mu_n B$, where μ_n is the neutron magnetic moment $(\mu_n = 60 \,\text{neV/T})$ [21]. Let v_{\parallel}^c be the critical longitudinal velocity that fulfills this requirement, given by $v_{\parallel}^{c} = \sqrt{2\mu_{n}B/m_{n}}.$

There is another factor that contributes to the transmission of UCN through the PM. If there is a spin-depolarizing region upstream of the PM (for example, we have gate valves made of stainless steel) and if the population of low-field seekers exceeds that of high-field seekers in the region upstream of the PM, which in turn is caused by low-field seekers being reflected by the PM potential (resulting in low f_{ℓ}), there is a chance for low-field seekers to be spin-flipped and pass through the PM as high-field seekers. We can rewrite Eq. (4) as

$$\frac{dN_1}{dv} = \frac{1}{2} \frac{dN_0}{dv} \left[f_h + f_\ell + \beta \left(f_h - f_\ell \right) \right] \tag{5}$$

where β is a free parameter that effectively describes this spinflipping effect.

We now describe expressions for f_h and f_ℓ . For the nowindow case $f_h = 1/2$, because half of the UCN in some velocity distribution dN_0/dv is directed upstream, away from the PM region.

 f_{ℓ} is a function of velocity that is dependent on the angular distribution of the UCN upstream of the PM and the strength of the PM field. For an isotropic velocity distribution, the fraction of low field seekers allowed through the PM is

$$f_{\ell} = \frac{2\pi \int_0^{\theta_c} d\theta \sin \theta}{4\pi} = \frac{1}{2} (1 - \cos \theta_c)$$
 (6)

$$= \frac{1}{2} \left(1 - \frac{v_{\parallel}^c}{v} \right) \quad \text{for } v > v_{\parallel}^c$$
 (7)

The limits of integration in the numerator were determined using the requirement $\cos \theta > v_c^{\parallel}/v$ for low-field seeking neutrons.

As UCN are transported from the source to the experiment through the guide system, the angular distribution becomes more forward directed. For a completely forward directed population of low-field seekers, we have $f_\ell=1/2$ for $\nu>\nu_\parallel^c$ and $f_\ell=0$ otherwise. The angular distribution is likely to be somewhere in between. We write a more general expression for f_ℓ with a free parameter characterizing the angular distribution of low field seeking neutrons

$$f_{\ell} = \frac{1}{2} \left(1 - k \left(\frac{v_{\parallel}^{c}}{v} \right) \right) \quad \text{for } v > v_{\parallel}^{c}$$
 (8)

where as k approaches 0, the UCN velocity distribution becomes forward directed, and as k approaches 1 the velocity distribution becomes isotropic.

We now describe a set of equations that can be used to fit UCN storage curves in a precession cell

$$N(t) = C \int_{\nu_{\text{low}}}^{\nu_{\text{high}}} d\nu \frac{dN_1}{d\nu} e^{-\frac{t}{\tau(\nu',\bar{\mu})}}$$

$$\frac{1}{\tau(\nu',\bar{\mu})} = \frac{1}{\tau_B} + \frac{A\nu'}{4 \text{ Vol}} \bar{\mu}$$
(10)

$$\bar{\mu} = 2\mu \left[\frac{V_{\text{Fermi}}^{\text{cell}}}{K(v')} \sin^{-1} \left(\frac{K(v')}{V_{\text{Fermi}}^{\text{cell}}} \right)^{1/2} - \left(\frac{V_{\text{Fermi}}^{\text{cell}}}{K(v')} - 1 \right)^{1/2} \right]$$
(11)

$$\frac{dN_1}{dv} = \frac{1}{2}v^{\alpha} \left[\frac{1}{2} + f_{\ell} + \beta \left(\frac{1}{2} - f_{\ell} \right) \right]$$

$$f_{\ell} = \begin{cases} \frac{1}{2} \left(1 - k \left(\frac{v_{\parallel}^{c}}{v} \right) \right) & \text{for } v > v_{\parallel}^{c} \text{ where } v_{\parallel}^{c} = \sqrt{2\mu_{N}B/m_{N}} \\ 0 & \text{otherwise} \end{cases}$$
(12)

with free parameters C, μ (velocity-dependent loss per bounce within the precession cell), β (upstream depolarization probability), α (velocity distribution), and k (angular distribution).

The lower integration limit of Eq. (9), v_{low} , is obtained from the potential U, the minimum energy of UCN required to enter a precession cell located above beam height. The velocity of UCN that have entered the cell, v', is related to v by $v' = \sqrt{v^2 - 2U/m_n}$. The term in the upper integration limit, v_{high} , is the velocity equivalent of $\min(V_{\text{Fermi}}^{\text{cell}} + U, V_{\text{Fermi}}^{\text{guide}})$, which is the maximum UCN energy from the input spectrum that is containable by either the transport guide (with material Fermi potential $V_{\text{Fermi}}^{\text{guide}}$) or the precession cell (with material Fermi potential $V_{\text{Fermi}}^{\text{guide}}$). Equation (10) describes the decay time of a stored UCN, which consists of the the free neutron lifetime τ_{β} with a velocity-dependent loss per bounce within the precession cell, where we assume that neutron velocity within the cell is isotropic. A is the inner surface area of the precession cell, and Vol is the volume of the precession cell. Equation (11), which describes loss per bounce, is taken from Eq. 2.70 in Ref. [2], where K(v') is the kinetic energy of the neutron in the cell. Note

that we assume that the UCN spectrum is not affected by the transport between the exit of the PM and the UCN precession cell. Therefore dN_1/dv also represents the input UCN velocity spectrum of UCN in the guide that arrive at the cell.

The holding curve formalism described by Eq. (9) - (13) can also be modified to account for the presence of the Al window in the PM region. We maintain the base form of Eq. (5), but now must alter our expressions for f_{ℓ} and f_{h} to account for the step potential represented by the window, which for Al we approximate to be 54 neV [2]. Low-field seekers must now have a high enough velocity to overcome both the PM field potential and the Al window step potential.

High-field seekers must also have a high enough velocity to overcome the window step potential, but receive the benefit of being accelerated by the PM field. When the energy increase from the PM field is greater than the Fermi potential of the window, high-field seekers of any velocity are transmitted through the window.

We now rewrite Eq. (14) - (19) to describe UCN storage curves with an Al window in the PM region.

$$N(t) = C \int_{v_h}^{v_{\text{high}}} dv \frac{dN_1}{dv} e^{-\frac{t}{\tau(v',\vec{\mu})}}$$
(14)

$$\frac{1}{\tau(\nu',\bar{\mu})} = \frac{1}{\tau_B} + \frac{A\nu'}{4\operatorname{Vol}}\bar{\mu} \tag{15}$$

$$\bar{\mu} = 2\mu \left[\frac{V_{\text{Fermi}}^{\text{cell}}}{K(\nu')} \sin^{-1} \left(\frac{K(\nu')}{V_{\text{Fermi}}^{\text{cell}}} \right)^{1/2} - \left(\frac{V_{\text{Fermi}}^{\text{cell}}}{K(\nu')} - 1 \right)^{1/2} \right]$$
(16)

$$\frac{dN_1}{dv} = \frac{1}{2}v^{\alpha} \left[f_h + f_{\ell} + \beta \left(f_h - f_{\ell} \right) \right] \tag{17}$$

$$f_{\ell} = \begin{cases} \frac{1}{2} \left(1 - k \frac{v_{\parallel}^{c}}{v} \right) & \text{for } v > v_{\parallel}^{c} \text{ where } \frac{1}{2} m \left(v_{\parallel}^{c} \right)^{2} = V_{\text{F}}^{\text{Al}} + \mu B \\ 0 & \text{otherwise} \end{cases}$$

 $f_{h} = \begin{cases} \frac{1}{2} \left(1 - k \frac{v_{\parallel}^{c}}{v} \right) & \text{for } v > v_{\parallel}^{c} \text{ where } \frac{1}{2} m \left(v_{\parallel}^{c} \right)^{2} = V_{\text{F}}^{\text{Al}} - \mu B \\ & \text{and } V_{\text{F}}^{\text{Al}} > \mu B \\ 0 & \text{for } v \leq v_{\parallel}^{c} \text{ where } \frac{1}{2} m \left(v_{\parallel}^{c} \right)^{2} = V_{\text{F}}^{\text{Al}} - \mu B \\ & \text{and } V_{\text{F}}^{\text{Al}} > \mu B \\ \frac{1}{2} & \text{for } V_{\text{F}}^{\text{Al}} \leq \mu B \end{cases}$ (19)

This formalism enables a fit of both no-window and withwindow UCN storage curves using the same set of free parameters.

4.2.1. Multi-parameter fits of UCN storage curves

Multi-parameter least square minimization fits were performed using the LMFIT Python library [22]. The results are presented in Tab. 2. For measurements with no window in the PM region, we fit Eq. (9) - (13), and for the measurements with a window present we fit Eq. (14) - (19). It should be noted that the bottom of the prototype cell was located 10 cm

above beam height. Therefore for NiP-coated Al wall run conditions we used an integration limits $v_{\rm low}$ and $v_{\rm high}$ as determined by U=10 neV and $V_{\rm Fermi}^{\rm guide}=214$ neV [18]. For dPS-coated PMMA wall run conditions we used U=10 neV and $V_{\rm Fermi}^{\rm cell}=160$ neV.

For run condition 4, we used a single effective loss per bounce parameter μ even though the cell was made of two different materials (i.e. dPS-coated cell wall with NiP electrodes). The reason for this was because the data did not have the sensitivity to resolve two separate μ values. This also applies to the simultaneous fit for data from run conditions 3 and 4.

4.3. Spin dependent UCN flux rate as a function of the polarizing magnet field

A flow-through measurement as described in section 3.2 was taken to obtain information on the input UCN spectrum. The switcher was set to channel polarized UCN from the PM directly into the spin analyzer and detector. For the duration of the measurement, the strength of the PM was slowly increased from 0 to 5 T and the spin flipper was toggled on and off at regular intervals (as per section 3.2). The Al window was present in the PM region for this measurement.

The flow-through measurement provides two curves describing neutron flux rate for each spin state as a function of the PM field strength (see Fig. 14). These curves can be fit using the formalism described in section 4.2.1 with modification to account for finite efficiency of the spin analyzer and spin flipper

Beginning from our equation for dN_1/dv , we write

$$\frac{dN_1}{dv} = \frac{1}{2}v^{\alpha} \left[f_h + f_\ell + \beta \left(f_h - f_\ell \right) \right] \tag{20}$$

and dividing this into expressions for low-field seekers and high-field seekers

$$\frac{dN_{1,\ell}}{d\nu} = \frac{1}{2}\nu^{\alpha}f_{\ell} = \frac{1}{2}\nu^{\alpha}f_{\ell D} \tag{21}$$

$$\frac{dv}{dv} = \frac{2}{2}v^{\alpha} \left[f_h + \beta \left(f_h - f_{\ell} \right) \right] = \frac{1}{2}v^{\alpha} f_{hD}$$
 (22)

where $f_{\ell D} = f_{\ell}$ and $f_{hD} = f_h + \beta (f_h - f_{\ell})$ describe the fraction of low-field seekers and high-field seekers downstream of the PM, respectively.

For spin analyzer efficiency A, when the spin flipper is off, there is some fraction of low-field seekers that are transmitted by the analyzing foil. Assuming that there is a negligible chance of depolarization downstream of the PM, dN_1/dv becomes

$$\frac{dN_{\text{off}}}{dv} = \frac{1}{2}v^{\alpha} \left[A f_{hD} + (1 - A)f_{\ell D} \right]$$
 (23)

When the spin flipper is on, for spin flipping power S, dN_1/dv becomes

$$\frac{dN_{\text{on}}}{dv} = \frac{1}{2}v^{\alpha} [A S f_{\ell D} + A(1 - S)f_{hD} + (1 - A)S f_{hD} + (1 - A)(1 - S)f_{\ell D}]$$
(24)

In the above equation, the first term describes low-field seekers downstream of the PM that are successfully spin flipped to high-field seekers and allowed through the spin analyzer. The second term is the fraction of high-field seekers that were not flipped and allowed through the spin analyzer. The third term is the fraction of high-field seekers that were flipped to low-field seekers, but allowed through to the detector due to finite analyzing power of the foil. The fourth term is the fraction of low-field seekers that were not spin flipped, but allowed through the spin analyzer due to finite analyzing power.

Following Ref. [19], we assume a spin analyzing power of A = 0.99 for UCN in the energy range of the LANL nEDM experiment and a magnetized iron foil spin analyzer.

Spin flipping power S can be estimated as follows. With UCN in a flow-through mode from the source to the detector and with the PM at 5 T, when the spin flipper was turned on, detected UCN flux rate was reduced to 12% compared to when the spin flipper was off, which corresponds to the ratio of Eq. (24) to Eq. (23). Assuming negligible depolarization downstream of the PM, this means $f_{\ell D}=0$ and $f_{hD}=1/2$. Letting A=0.99 and solving for S yields a spin flipping power of S=0.89.

The spin-flipper-off and spin-flipper-on curves were fit using an integral of $dN_{\rm off}/dv$ and $dN_{\rm on}/dv$, respectively, with limits of integration from 0 m/s to 7.58 m/s (the velocity equivalent of UCN in a 5 T field). This fit is shown in Fig. 14, with the fit parameters from Tab. 3.

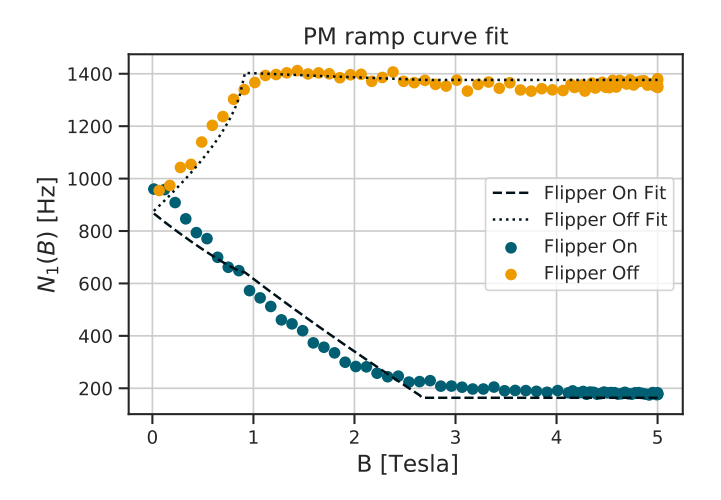


Figure 14: A measurement of neutron transmission from the source to the dropdetector with the B field of the PM decreasing from 5 T to 0 T over the course of 72 minutes, with the spin flipper toggling on and off. This generates two curves that are describable using Eq. (23) and (24), which share the same set of free parameters as Eq. (14) – (19). The results of a simultaneous fit of these PM ramping curves are listed in Tab. 3

5. Discussion

As measured in run condition 4, Fig. 13, a storage time of 180 s in a single cell yields a UCN count of $\sim 60,000$ UCN, well in excess of the number required to reach the desired statistical uncertainty. In Ref. [15], $\alpha = 0.8$, $E = 12 \, \text{kV/cm}$, $T_{\rm fp} = 180 \, \text{s}$, N = 39,000 for each cell, and $T_{\rm cycle} = 300 \, \text{s}$

Table 2: Multi-parameter fits of UCN storage curves. Refer to Tab. 1 for run condition details.

Run	1	2	3	4	3 & 4	
$C/10^3$	2(1)	3(1)	5(3)	5(3)	4(1) 7(2)	
α	3.0(3)	2.5(2)	2.5(3)	2.7(2)	2.6(2)	
β	0.30(2)	0.8(2)	0.6(3)	0.8(2)	0.77(17)	
k	0.3(1)	0.6(1)	0.7(1)	0.5(1)	0.6(1)	
$\mu/10^{-4}$	2.0(1)	2.6(2)	3.5(4)	3.1(2)	3.4(2)	
$Corr(C, \alpha)$	-1	-0.94	-0.96	-0.96	-0.97 -0.96	
$Corr(C, \beta)$	-0.2	-0.32	-0.4	-0.5	-0.49 -0.53	
Corr(C, k)	-0.7	-0.14	-0.14	0.02	-0.16 -0.12	
$Corr(C, \mu)$	0.9	0.85	0.77	0.79	0.78 0.76	
$Corr(\alpha, \beta)$	-0.2	0.01	0.15	0.27	0.23	
$Corr(\alpha, k)$	0.71	0.44	0.37	0.22	0.41	
$Corr(\alpha, \mu)$	-0.97	-0.92	-0.84	-0.83	-0.82	
$Corr(\beta, k)$	-0.33	-0.86	-0.81	-0.83	-0.72	
$Corr(\beta, \mu)$	0.21	0.14	0.16	-0.03	0.01	
$Corr(k, \mu)$	-0.6	-0.56	-0.63	-0.41	-0.57	
$Corr(C_3, C_4)$					1	

Table 3: Multi-parameter fit of a PM ramp

Run condition	α	β	k
With Al window, UCN-flow through mode	1.0(1)	0.00(5)	0.30(2)

were assumed to arrive at an estimated statistical uncertainty of $\sigma_{d_n} = 4.0 \times 10^{-26} e \cdot \text{cm}$ per day with a double cell geometry. With an assumed data taking efficiency of 50% (for experiment down time, calibration and systematic studies) and the nominal LANSCE accelerator running schedule, this corresponds to a statistical uncertainty of $\sigma_{d_n} = 2.1 \times 10^{-27} e \cdot \text{cm}$ in 5 calendar years. The number of stored polarized UCN observed was about 50% larger than what was reported in a similar measurement performed on the West Beamline [15]. We attribute the improvement to the better switcher transmission in spite of the longer transport distance.

Additionally, we have demonstrated the utility of a UCN storage curve model. Varying the strength of the PM for UCN storage curves allowed the properties of a continuous UCN input energy spectrum on the North Beamline to be obtained. Importantly, the model describes both window-in and window-out storage with the same input parameters.

We can draw a number of observations from the results of the UCN storage curves fits depicted in Tab. 2. First, the value of C in run conditions 3 and 4 is larger than the value in run condition 2, showing that the new rotary switcher transports a larger number of UCN than the old prototype switcher. Second, k (ranging from 0.3(1) to 0.7(1)) across all run conditions indicates that the angular distribution of the input UCN velocity spectrum on the beamline is relatively forward directed. Third, β is \sim 0.7 for run conditions with the Al window and is \sim 0.3 for the run condition without the window. This is consistent with the idea that the presence of the Al window reduces the number of low-field seeking UCN that pass the PM region, resulting in an increased chance for a low-field seeker to see a depolarizing region upstream of the PM and an effectively larger β . Com-

paratively, in the no window case, more low-field seekers pass the PM region, lowering the chance for a low-field seeker to be depolarized and giving a smaller value for β .

In some cases there are rather large correlations among parameters as seen in Tab. 2. The largest parameter correlations for fits across all run conditions are $Cor(C,\alpha) \sim -1$, $Cor(\alpha,\mu) \sim -0.9$, and $Cor(C,\mu) \sim 0.8$. Special care was taken in the least-squares fitting process to choose initial parameter guesses for α and μ that were based on previous measurements along the West Beamline (see Ref. [15, 18]) because of these correlations. As a result, we obtained $\alpha \sim 3$ and $\mu \sim 3 \times 10^{-4}$ across all run conditions.

It can be seen in Fig. 10 that the storage curve model reproduces the storage curves at various PM field strengths for configurations without a window. For configurations with a window in the PM region (Fig. 11-13), the holding curve model reproduces the storage curves for holding times less than $200 \, \mathrm{s}$. For longer holding times (> $200 \, \mathrm{s}$) in run conditions with the PM window, the holding curve model overpredicts the number of UCN. We postulate that there is an additional mechanism caused by the presence of the window that preferentially selects for higher energy UCN to enter the precession cell. Higher energy UCN experience more wall collisions within the precession cell, and are more likely to be lost during the storage period.

One possible mechanism is bulk scattering of UCN within the PM window caused by nonuniformities within the window material. The magnetic field accelerates high-field seeking UCN through the Al window. If the window scatters the UCN, then a fraction of the longitudinal velocity (i.e. along the direction of the beamline) results in a transverse velocity component. Lower energy UCN may lose enough longitudinal velocity and become trapped in the the PM field potential well, a process less likely for higher energy UCN.

Lastly, we have shown that elements of the holding curve model may be adapted to a UCN flow-through measurement through a PM with an Al window, while the PM slowly ramps up or down. We observe that the model is able to reproduce the major features of the data (Fig. 14). As the B field increases, low-field seekers are reflected by the potential well of the PM. Conversely, the fraction of high field seekers allowed past the Al window slowly increases with the strength of the B field, until the strength of the B field reaches a threshold where all highfield seekers are accelerated past the window region. The parameters of the model, presented in Tab. 3, indicate a forwarddirected angular distribution (k = 0.30(2)) consistent with the holding curve fits in Tab. 2. The estimate of $\beta = 0$ is also consistent with what we expect, because UCN in a flow-through measurement with no preload period have less opportunity to be depolarized upstream of the PM.

The precision for α in Tab. 3 is limited due the change in the UCN energy spectrum during the course of the flow-through measurement. During the 72 min required to ramp the PM, the continued use of the UCN source causes heating and a corresponding change in the input energy spectrum [23]. Note that the measurement depicted in Fig. 14 was a PM ramp down sequence, where the field was decreased from 5 T to 0 T. Therefore, a worse fit of the model in the 0 T to 1 T region is expected.

6. Conclusion

We have demonstrated successful instrumentation of a prototype precession cell, single-channel spin analyzer, spin flipper, UCN detector, and rotary switcher for UCN transport in preparation for the LANL nEDM experiment. Approximately 60,000 UCN, sufficient to obtain a statistical uncertainty of $\delta d_n = 2 \times 10^{-27} \ e \cdot \text{cm}$ for the nEDM have been stored in a prototype cell with dPS-coated PMMA walls and NiP-coated Al electrode plates. An analytical model has been developed that describes various properties of the UCN exiting the PM that affect the performance of experiments that use UCN. These properties include depolarization in the beamline upstream of the PM, the UCN velocity spectrum, and the angular distribution of the UCN. We have successfully applied this model to the analysis of a series of UCN storage curves taken with prototype precession cells of the LANL nEDM experiment and data on UCN transmission through the PM. The extracted UCN velocity spectrum can be used to analyze and optimize the performance of the LANL nEDM experiment.

Acknowledgments

This work was supported by Los Alamos National Laboratory LDRD Program (Project No. 20190041DR), the U.S. National Science Foundation (Grant No. PHY-1828512 (Indiana U.) and Grant No. PHY-2110988 (U. Michigan)), and the

U.S. Department of Energy, Office of Science, Office of Workforce Development for Teachers and Scientists, Office of Science Graduate Student Research (SCGSR) program (Contract No. DE-SC0014664). We gratefully acknowledge the support provided by the LANL Physics and AOT Divisions.

References

- V. Ignatovich, G. Pontecorvo, The Physics of Ultracold Neutrons, Oxford science publications, Clarendon Press, 1990.
- [2] R. Golub, D. Richardson, S. Lamoreaux, Ultra-Cold Neutrons, CRC Press, 1991.
- [3] D. Dubbers, M. G. Schmidt, The neutron and its role in cosmology and particle physics, Rev. Mod. Phys. 83 (2011) 1111-1171. doi:10.1103/ RevModPhys.83.1111.
- [4] A. R. Young, S. Clayton, B. W. Filippone, P. Geltenbort, T. M. Ito, C.-Y. Liu, M. Makela, C. L. Morris, B. Plaster, A. Saunders, S. J. Seestrom, R. B. Vogelaar, Beta decay measurements with ultracold neutrons: a review of recent measurements and the research program at los alamos national laboratory, Journal of Physics G: Nuclear and Particle Physics 41 (2014) 114007. doi:10.1088/0954-3899/41/11/114007.
- [5] C. A. Baker, D. D. Doyle, P. Geltenbort, K. Green, M. G. D. van der Grinten, P. G. Harris, P. Iaydjiev, S. N. Ivanov, D. J. R. May, J. M. Pendlebury, J. D. Richardson, D. Shiers, K. F. Smith, Improved experimental limit on the electric dipole moment of the neutron, Phys. Rev. Lett. 97 (2006) 131801. URL: https://link.aps.org/doi/10.1103/PhysRevLett.97.131801. doi:10.1103/PhysRevLett.97.131801.
- [6] C. Abel, S. Afach, N. J. Ayres, C. A. Baker, G. Ban, G. Bison, K. Bodek, V. Bondar, M. Burghoff, E. Chanel, Z. Chowdhuri, P.-J. Chiu, B. Clement, C. B. Crawford, M. Daum, S. Emmenegger, L. Ferraris-Bouchez, M. Fertl, P. Flaux, B. Franke, A. Fratangelo, P. Geltenbort, K. Green, W. C. Griffith, M. van der Grinten, Z. D. Grujić, P. G. Harris, L. Hayen, W. Heil, R. Henneck, V. Hélaine, N. Hild, Z. Hodge, M. Horras, P. Iaydjiev, S. N. Ivanov, M. Kasprzak, Y. Kermaidic, K. Kirch, A. Knecht, P. Knowles, H.-C. Koch, P. A. Koss, S. Komposch, A. Kozela, A. Kraft, J. Krempel, M. Kuźniak, B. Lauss, T. Lefort, Y. Lemière, A. Leredde, P. Mohanmurthy, A. Mtchedlishvili, M. Musgrave, O. Naviliat-Cuncic, D. Pais, F. M. Piegsa, E. Pierre, G. Pignol, C. Plonka-Spehr, P. N. Prashanth, G. Quéméner, M. Rawlik, D. Rebreyend, I. Rienäcker, D. Ries, S. Roccia, G. Rogel, D. Rozpedzik, A. Schnabel, P. Schmidt-Wellenburg, N. Severijns, D. Shiers, R. Tavakoli Dinani, J. A. Thorne, R. Virot, J. Voigt, A. Weis, E. Wursten, G. Wyszynski, J. Zejma, J. Zenner, G. Zsigmond, Measurement of the permanent electric dipole moment of the neutron, Phys. Rev. Lett. 124 (2020) 081803. URL: https://link.aps.org/doi/10. 1103/PhysRevLett.124.081803. doi:10.1103/PhysRevLett.124. 081803.
- [7] M. Pospelov, A. Ritz, Electric dipole moments as probes of new physics, Annals of Physics 318 (2005) 119-169. URL: https://www.sciencedirect.com/science/article/pii/ S0003491605000539. doi:https://doi.org/10.1016/j.aop. 2005.04.002, special Issue.
- [8] J. Engel, M. J. Ramsey-Musolf, U. van Kolck, Electric dipole moments of nucleons, nuclei, and atoms: The standard model and beyond, Progress in Particle and Nuclear Physics 71 (2013) 21-74. URL: https://www.sciencedirect.com/science/article/pii/ S0146641013000227. doi:https://doi.org/10.1016/j.ppnp. 2013.03.003, fundamental Symmetries in the Era of the LHC.
- [9] T. Chupp, M. Ramsey-Musolf, Electric dipole moments: A global analysis, Phys. Rev. C 91 (2015) 035502. URL: https://link.aps.org/doi/10.1103/PhysRevC.91.035502. doi:10.1103/PhysRevC.91.035502.
- [10] V. Cirigliano, Y. Li, S. Profumo, M. J. Ramsey-Musolf, Mssm baryogenesis and electric dipole moments: an update on the phenomenology, Journal of High Energy Physics 2010 (2010) 2. URL: https://doi.org/10.1007/JHEP01(2010)002. doi:10.1007/JHEP01(2010)002.
- [11] D. E. Morrissey, M. J. Ramsey-Musolf, Electroweak baryogenesis, New Journal of Physics 14 (2012) 125003. URL: https://doi.org/10.1088/1367-2630/14/12/125003. doi:10.1088/1367-2630/14/12/125003.

- [12] F. M. Piegsa, New concept for a neutron electric dipole moment search using a pulsed beam, Phys. Rev. C 88 (2013) 045502. URL: https:// link.aps.org/doi/10.1103/PhysRevC.88.045502. doi:10.1103/ PhysRevC.88.045502.
- [13] R. Alarcon, J. Alexander, V. Anastassopoulos, T. Aoki, R. Baartman, S. Baeßler, L. Bartoszek, D. H. Beck, F. Bedeschi, R. Berger, M. Berz, H. L. Bethlem, T. Bhattacharya, M. Blaskiewicz, T. Blum, T. Bowcock, A. Borschevsky, K. Brown, D. Budker, S. Burdin, B. C. Casey, G. Casse, G. Cantatore, L. Cheng, T. Chupp, V. Cianciolo, V. Cirigliano, S. M. Clayton, C. Crawford, B. P. Das, H. Davoudiasl, J. de Vries, D. DeMille, D. Denisov, M. V. Diwan, J. M. Doyle, J. Engel, G. Fanourakis, R. Fatemi, B. W. Filippone, V. V. Flambaum, T. Fleig, N. Fomin, W. Fischer, G. Gabrielse, R. F. G. Ruiz, A. Gardikiotis, C. Gatti, A. Geraci, J. Gooding, B. Golub, P. Graham, F. Gray, W. C. Griffith, S. Haciomeroglu, G. Gwinner, S. Hoekstra, G. H. Hoffstaetter, H. Huang, N. R. Hutzler, M. Incagli, T. M. Ito, T. Izubuchi, A. M. Jayich, H. Jeong, D. Kaplan, M. Karuza, D. Kawall, O. Kim, I. Koop, W. Korsch, E. Korobkina, V. Lebedev, J. Lee, S. Lee, R. Lehnert, K. K. H. Leung, C.-Y. Liu, J. Long, A. Lusiani, W. J. Marciano, M. Maroudas, A. Matlashov, N. Matsumoto, R. Mawhorter, F. Meot, E. Mereghetti, J. P. Miller, W. M. Morse, J. Mott, Z. Omarov, L. A. Orozco, C. M. O'Shaughnessy, C. Ozben, S. Park, R. W. Pattie, A. N. Petrov, G. M. Piacentino, B. R. Plaster, B. Podobedov, M. Poelker, D. Pocanic, V. S. Prasannaa, J. Price, M. J. Ramsey-Musolf, D. Raparia, S. Rajendran, M. Reece, A. Reid, S. Rescia, A. Ritz, B. L. Roberts, M. S. Safronova, Y. Sakemi, P. Schmidt-Wellenburg, A. Shindler, Y. K. Semertzidis, A. Silenko, J. T. Singh, L. V. Skripnikov, A. Soni, E. Stephenson, R. Suleiman, A. Sunaga, M. Syphers, S. Syritsyn, M. R. Tarbutt, P. Thoerngren, R. G. E. Timmermans, V. Tishchenko, A. V. Titov, N. Tsoupas, S. Tzamarias, A. Variola, G. Venanzoni, E. Vilella, J. Vossebeld, P. Winter, E. Won, A. Zelenski, T. Zelevinsky, Y. Zhou, K. Zioutas, Electric dipole moments and the search for new physics, 2022. URL: https://arxiv.org/abs/2203. 08103. doi:10.48550/ARXIV.2203.08103.
- [14] N. F. Ramsey, A Molecular Beam Resonance Method with Separated Oscillating Fields, Physical Review 78 (1950) 695–699. doi:10.1103/ PhysRev.78.695, publisher: American Physical Society.
- [15] T. M. Ito, E. R. Adamek, N. B. Callahan, J. H. Choi, S. M. Clayton, C. Cude-Woods, S. Currie, X. Ding, D. E. Fellers, P. Geltenbort, S. K. Lamoreaux, C. Y. Liu, S. MacDonald, M. Makela, C. L. Morris, R. W. Pattie Jr., J. C. Ramsey, D. J. Salvat, A. Saunders, E. I. Sharapov, S. Sjue, A. P. Sprow, Z. Tang, H. L. Weaver, W. Wei, A. R. Young, Performance of the upgraded ultracold neutron source at Los Alamos National Laboratory and its implication for a possible neutron electric dipole moment experiment, Physical Review C 97 (2018) 012501. doi:10.1103/PhysRevC.97.012501.
- [16] Z. Wang, C. Morris, Multi-layer boron thin-film detectors for neutrons, Nuclear Instruments and Methods in Physics Research Section A: Accelerators, Spectrometers, Detectors and Associated Equipment 652 (2011) 323–325. doi:10.1016/j.nima.2011.01.138.
- [17] Z. Tang, E. Adamek, A. Brandt, N. Callahan, S. Clayton, S. Currie, T. Ito, M. Makela, Y. Masuda, C. Morris, R. Pattie, J. Ramsey, D. Salvat, A. Saunders, A. Young, Measurement of spin-flip probabilities for ultra-cold neutrons interacting with nickel phosphorus coated surfaces, Nuclear Instruments and Methods in Physics Research Section A: Accelerators, Spectrometers, Detectors and Associated Equipment 827 (2016) 32–38. doi:10.1016/j.nima.2016.04.098.
- [18] R. W. Pattie Jr, E. Adamek, T. Brenner, A. Brandt, L. J. Broussard, N. B. Callahan, S. M. Clayton, C. Cude-Woods, S. A. Currie, P. Geltonbort, T. Ito, T. Lauer, C. Y. Liu, J. Majewski, M. Makela, Y. Masuda, C. L. Morris, J. C. Ramsey, D. Salvat, A. Saunders, J. Schroffenegger, Z. Tang, W. Wei, Z. Wang, E. Watkins, A. R. Young, B. A. Zeck, Evaluation of commercial nickel-phosphorus coating for ultracold neutron guides using a pinhole bottling method, Nuclear Instruments and Methods in Physics Research Section A: Accelerators, Spectrometers, Detectors and Associated Equipment 872 (2017) 64–73. doi:10.1016/j.nima.2017.07.051.
- [19] T. S. Zechlau, Ultra-Cold Neutron Transport and Spin Manipulation System for the Measurement of the Neutron Electric Dipole Moment, Dissertation, Technische Universität München, München, 2016.
- [20] A. T. Holley, L. J. Broussard, J. L. Davis, K. Hickerson, T. M. Ito, C.-Y. Liu, J. T. M. Lyles, M. Makela, R. R. Mammei, M. P. Mendenhall, C. L.

- Morris, R. Mortensen, R. W. Pattie, R. Rios, A. Saunders, A. R. Young, A high-field adiabatic fast passage ultracold neutron spin flipper for the UCNA experiment, Review of Scientific Instruments 83 (2012) 073505. doi:10.1063/1.4732822.
- [21] E. Tiesinga, P. J. Mohr, D. B. Newell, B. N. Taylor, Codata recommended values of the fundamental physical constants: 2018, Rev. Mod. Phys. 93 (2021) 025010. doi:10.1103/RevModPhys.93.025010.
- [22] M. Newville, T. Stensitzki, D. B. Allen, A. Ingargiola, LMFIT: Non-Linear Least-Square Minimization and Curve-Fitting for Python, 2014. doi:10.5281/zenodo.11813.
- [23] A. Anghel, T. L. Bailey, G. Bison, B. Blau, L. J. Broussard, S. M. Clayton, C. Cude-Woods, M. Daum, A. Hawari, N. Hild, P. Huffman, T. M. Ito, K. Kirch, E. Korobkina, B. Lauss, K. Leung, E. M. Lutz, M. Makela, G. Medlin, C. L. Morris, R. W. Pattie, D. Ries, A. Saunders, P. Schmidt-Wellenburg, V. Talanov, A. R. Young, B. Wehring, C. White, M. Wohlmuther, G. Zsigmond, Solid deuterium surface degradation at ultracold neutron sources, The European Physical Journal A 54 (2018) 148. URL: http://link.springer.com/10.1140/epja/i2018-12594-2. doi:10.1140/epja/i2018-12594-2.